RSC Advances

PAPER

View Article Online
View Journal | View Issue

Cite this: RSC Adv., 2016, 6, 67525

Growth of $Ba_{1-x}Sr_xZrO_3$ ($0 \leq x \leq 1$) nanoparticles in supercritical water†

Akira Yoko,*[a] Makoto Akizuki,[a] Naoto Umezawa,[b] Takahisa Ohno[b] and Yoshito Oshima[a]

We studied the formation of $Ba_{1-x}Sr_xZrO_3$ ($0 \leq x \leq 1$) nanoparticles under highly super-saturated conditions, using supercritical water. It is known that B-site Zr in the perovskite structure plays a dominant role at the nucleation stage, with high nucleation rates under supercritical conditions; this is due to the significantly lower solubility of Zr, compared with A-site ions (*i.e.*, Zr precipitates faster, and A-site ions are taken up into particle after the Zr nucleation). However, in this study, it was found that A-site Ba and Sr significantly influenced the particle size, the A-site deficiency rate, and the surface-OH density of the nanoparticles. The differences in particle size suggested that the ripening or coalescence that occurred after the nucleation stage was dominant in determining the particle size, even under highly super-saturated conditions such as those realized in the supercritical hydrothermal synthesis. The characteristic nanostructure formed in the supercritical water was analyzed in detail; variables such as the A-site deficiency rate and the surface-OH density were investigated. The existence of vacancies at the A-site was confirmed using X-ray absorption fine structure, and a highly defective structure was obtained, particularly when the Ba content was high. The surface state of the nanoparticles was also studied using X-ray photoelectron spectroscopy and first-principles calculations, with the aim of understanding the differences in particle size, and the effects of the A-site deficiencies; the amount of surface-OH corresponded to the A-site deficiency rate, and had an inverse relationship with the particle size.

Received 11th May 2016
Accepted 11th July 2016

DOI: 10.1039/c6ra12288d

www.rsc.org/advances

1. Introduction

Nanometer-scale control over the grain size is required for the realization of high-performance devices, and the miniaturization of such devices. The use of nanoparticles enables the production of dense and thin sintered ceramics, which are expected to be applied for devices such as capacitors, sensors, fuel cells, and secondary cells. Nanoparticles can be obtained with a narrow size distribution using solution-based synthesis methods, but not using conventional solid-state reaction synthesis; recently, various solution methods have been developed and studied. For example, Lee *et al.* compared luminescent materials synthesized using various synthetic methods, and the products of solution methods showed a higher photoluminescence emission intensity, because of the lower degree of aggregation, and more uniform particle size.[1] Granulation methods have a great effect on the particle size, morphology, and structure of materials, and the physical properties of materials are different when synthesized using different methodologies, even if the same starting materials are used.[2–6] Therefore, investigating a synthetic methodology through a detailed characterization of the products is essential for the discovery of new nanomaterials.

Supercritical hydrothermal synthesis is a solution method that can be applied for the synthesis of metal oxide nanoparticles with a narrow size distribution, and good crystallinity. Nanoparticles can be obtained using supercritical water, because of the acceleration of nucleation and the inhibition of ripening. High nucleation rates can be realized by using a high degree of super-saturation, and ripening can be suppressed *via* an extremely low solubility in supercritical water.[7] A high degree of super-saturation can be obtained when the temperature of the water is increased rapidly from a normal temperature to a temperature above the critical temperature; the low kinetic viscosity of supercritical water enables rapid mixing of fluids with a continuous flow reactor that leads to a rapid increase in water temperature. Higher-crystallinity particles can be obtained, compared with other solution methods, because of the higher reaction temperature. The high crystallinity of the synthesized particles means that the calcination post-processing that is required for conventional solution methods is not needed, or can be simplified, when supercritical hydrothermal methods are applied to perform granulation.[8]

[a]Department of Environment Systems, Graduate School of Frontier Sciences, The University of Tokyo, 5-1-5 Kashiwanoha, Kashiwa, Chiba 277-8563, Japan. E-mail: yoko@oshimalab.k.u-tokyo.ac.jp; Fax: +81 4 7136 4694; Tel: +81 4 7136 4694

[b]International Center for Materials Nanoarchitectonics (MANA), National Institute for Materials Science, 1-1 Namiki, Tsukuba, Ibaraki 305-0044, Japan

† Electronic supplementary information (ESI) available. See DOI: 10.1039/c6ra12288d

A distinctive feature of supercritical hydrothermal synthesis is the rapid crystallization that occurs as a result of the high degree of super-saturation. Semi-stable-state or non-equilibrium-state materials can be formed during such rapid structural formation; highly super-saturated conditions can affect the structural and compositional factors in addition to the particle size. For instance, we previously studied the supercritical hydrothermal synthesis of $BaZrO_3$, and discovered the formation of $BaZrO_3$, which had an extremely high concentration of deficiencies at the A-site in the first stage of crystallization.[9,10] The formation of nanoparticles in supercritical water with a similarly deficient structure was also reported in a previous study on the mechanism of formation of nickel ferrite.[11] The non-stoichiometry and defective structures observed in these studies can affect the properties of particles, and the structural analysis of nanoparticles formed in supercritical water is important. Particularly in the case of composite oxides, the non-stoichiometry and the deficient local structure becomes more crucial during the synthesis, because each element has a different driving force of crystallization, because of the differences in their solubility in water.

In this study, the supercritical hydrothermal synthesis of $Ba_{1-x}Sr_xZrO_3$ ($0 \leq x \leq 1$) was carried out, and structural analysis of the products was performed to elucidate the formation of the structure in the highly supersaturated reaction field. The perovskite-type oxides $BaZrO_3$ and $SrZrO_3$ are expected to find applications as proton conductors.[12–14] Composite oxides containing both Ba and Sr at the A-site show dielectric properties,[15–17] because the crystal structure of zirconate varies depending on its composition; some structural studies have also been conducted investigating the phase transition[18,19] and the thermal properties.[20]

We previously investigated the mechanism of formation of $BaZrO_3$ in supercritical hydrothermal synthesis, and observed the existence of a highly Ba-deficient perovskite structure, which is a characteristic of the methodology.[9,10] These results suggested that extraordinary structures could appear in supercritical water, due to the accelerated crystallization. Previous studies have shown that A-site-deficient perovskite oxide is important for a variety of applications. Several studies have been performed, including investigations of strontium niobium cobalt oxide ($Sr_{0.95}Nb_{0.1}Co_{0.9}O_{3-\delta}$) for low-temperature solid-oxide fuel cells,[21] the deficient effects of yttrium-doped barium cerate zirconate ($Ba_xCe_{0.5}Zr_{0.4}Y_{0.1}O_{3-\delta}$ ($x = 0.95$–1.05)) on sinterability and electrical conductivity,[22] gadolinium tantalite ($Gd_{1/3}TaO_3$) for lithium insertion reactions,[23,24] and barium lanthanum titanate ($Ba_{(1-x)/2}La_{x/3}TiO_3$ ($x = 0.1$–1.0)) for dielectric materials.[25] A detailed analysis of the products using X-ray diffraction (XRD), transmission electron microscopy energy-dispersive X-ray spectroscopy (TEM-EDX), X-ray photoelectron spectroscopy (XPS), X-ray absorption fine structure (XAFS), and first-principles calculations based on density functional theory (DFT), was conducted to investigate the mechanism of formation of $Ba_{1-x}Sr_xZrO_3$ ($0 \leq x \leq 1$) in supercritical water.

2. Experimental

2.1 Materials

Barium nitrate [$Ba(NO_3)_2$ (purchased from Kanto Chemical Co., Inc., Tokyo, Japan)], strontium nitrate [$Sr(NO_3)_2$ (purchased from Kanto Chemical Co., Inc., Tokyo, Japan)], and oxyzirconium nitrate [$ZrO(NO_3)_2 \cdot 2H_2O$ (purchased from Kanto Chemical Co., Inc., Tokyo, Japan)] were used as starting materials. Potassium hydroxide [KOH (purchased from Wako Pure Chemical Industries Ltd., Osaka, Japan)] was used as a base solution for tuning the pH. Nitric acid [HNO_3 (purchased from Wako Pure Chemical Industries Ltd., Osaka, Japan)] was used to neutralize the recovered solution. Distilled water (produced from RFD240HA; Advantec MFS, Inc., Tokyo, Japan) was used in the preparation of the feed solution. Table 1 shows the amounts of the starting materials used for the synthesis of $Ba_{1-x}Sr_xZrO_3$. An excess of Ba and Sr, relative to the amount of Zr (4 times), was used in the starting solutions to obtain mono-phase products following the previous study of $BaZrO_3$ formation;[9] otherwise ZrO_2 phase is also contained in products. The proportion of Ba and Sr in the starting solutions was changed as shown in Table 1 while the value of 4 for the ratio of A-site ions (Ba and Sr) *versus* Zr was maintained to avoid formation of ZrO_2 phase.

2.2 Methods

All experiments were performed using the continuous flow reactor illustrated in Fig. 1. Starting solutions of barium, strontium, and zirconium were simultaneously mixed with the base solution and heated distilled water, using a cross-shaped part (SUS316; inner diameter: 1.3 mm). The starting solution and

Table 1 Starting materials used for the $Ba_{1-x}Sr_xZrO_3$ synthesis

Ba starting material		Sr starting material		Zr starting material		Base solution		$\frac{(Ba+Sr)}{Zr}$	x
$Ba(NO_3)_2$	0.020 M	$Sr(NO_3)_2$	—	$ZrO(NO_3)_2$	0.005 M	KOH	0.05 M	4	0
$Ba(NO_3)_2$	0.015 M	$Sr(NO_3)_2$	0.005 M	$ZrO(NO_3)_2$	0.005 M	KOH	0.05 M	4	0.25
$Ba(NO_3)_2$	0.010 M	$Sr(NO_3)_2$	0.010 M	$ZrO(NO_3)_2$	0.005 M	KOH	0.05 M	4	0.50
$Ba(NO_3)_2$	0.009 M	$Sr(NO_3)_2$	0.011 M	$ZrO(NO_3)_2$	0.005 M	KOH	0.05 M	4	0.55
$Ba(NO_3)_2$	0.008 M	$Sr(NO_3)_2$	0.012 M	$ZrO(NO_3)_2$	0.005 M	KOH	0.05 M	4	0.60
$Ba(NO_3)_2$	0.007 M	$Sr(NO_3)_2$	0.013 M	$ZrO(NO_3)_2$	0.005 M	KOH	0.05 M	4	0.65
$Ba(NO_3)_2$	0.005 M	$Sr(NO_3)_2$	0.015 M	$ZrO(NO_3)_2$	0.005 M	KOH	0.05 M	4	0.75
$Ba(NO_3)_2$	—	$Sr(NO_3)_2$	0.020 M	$ZrO(NO_3)_2$	0.005 M	KOH	0.05 M	4	1

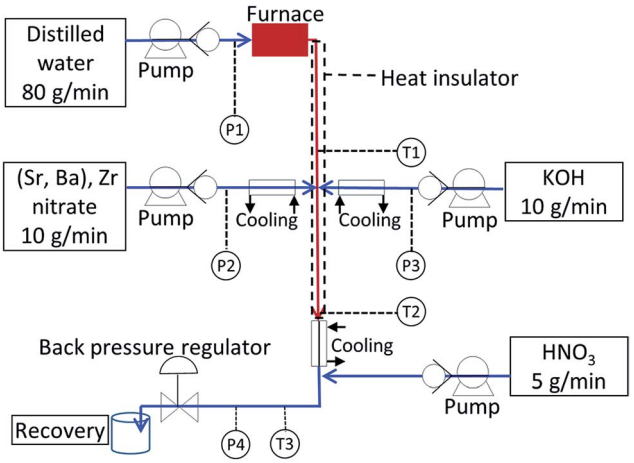

Fig. 1 Experimental setup for continuous flow reactor.

base solution were introduced into the reactor at a flow rate of 10 g min^{-1}, and heated distilled water was introduced at 80 g min^{-1} using a non-pulsation pump (NP-KX-500; Nihon Seimitsu Co., Ltd., Tokyo, Japan). The starting solution and the base solution were cooled just before the mixing point, to prevent warming of the starting solutions *via* conductive heat transfer before mixing. The flow rates set a Reynolds number (Re) of 4×10^4 at the reactor, just after mixing. Kawasaki *et al.* investigated the relationship between particle size and Re, and suggested that sufficient mixing was achieved at values of Re $\geq 4 \times 10^4$; at these values, the mixing conditions did not affect the particle size.[26] The temperature of the water was set at 400 °C at the point just before cooling (T_2 in Fig. 1). The pressure was set at 30 MPa using a back-pressure regulator (BP66-112865; Go Inc., Spartanburg, South Carolina, United states). The residence time was set at 0.9 s by the reactor volume from the mixing point to the point just before the cooling. After cooling, an HNO_3 solution was introduced using a flow rate of 5 g min^{-1}, to reconcile the pH and prevent formation of carbonate in the recovered dispersion.

The solid products were recovered *via* pressurized filtering using a nitrocellulose filter (VSWP14250; Merck Millipore Corporation, Darmstadt, Germany, pore size: 0.025 μm (we confirmed that single nanometer particles are also recovered by this filter)[9]), and were dried in a vacuum oven at room temperature (ADP-31; Yamato Corporation, Tokyo, Japan). The recovered particles and filtrate were analyzed as described below.

2.3 Analysis

The quantitative analysis of metal dissolved in the filtrate was conducted using inductively coupled plasma atomic emission spectroscopy (ICP-AES) (JY138KH; Horiba Ltd., Kyoto, Japan). The XRD measurements were conducted at room temperature using a powder diffractometer (SmartLab; Rigaku Corporation, Tokyo, Japan), with 0.005° step, using Cu Kα radiation (λ = 1.5406 Å), and Rietveld refinement was conducted to analyze the crystal structure using RIETAN-FP software.[27] TEM (JEM-2100; JEOL Ltd., Tokyo, Japan) was used to observe the size and morphology of the particles, and EDX combined with the TEM instrument was applied for single-particle composition analysis. Characteristic X-rays of $L\alpha_1$ for Ba (4.47 keV), $K\alpha_1$ for Sr (14.17 keV), and $K\beta_1$ for Zr (17.67 keV) were used for quantitative analysis, to eliminate mutual interference from each element. XPS was performed using a PHI 5000 VersaProbe (ULVAC-PHI Inc., Kanagawa, Japan) instrument to probe the surface state of the particles, using Al Kα as an X-ray source. XAFS was conducted at BL9C of Photon Factory, KEK, and the local structure that could not be obtained *via* diffraction was detected, and discussed with theoretical calculations using IFEFFIT software.[28]

2.4 First-principles calculations

2.4.1 Calculation conditions. First-principles calculations based on DFT were conducted, to obtain structural information and to support the experimental data. Projector-augmented wave pseudopotentials were employed as implemented in the VASP code.[29] The generalized-gradient approximation proposed by Perdew, Burke, and Ernzerhof (PBE)[30] represented the exchange–correlation energy functional.[20,21] The valence configurations of the pseudopotentials were $5s^2 5p^6 6s^2$ for Ba, $4s^2 4p^6 5s^2$ for Sr, $4s^2 4p^6 4d^2 5s^2$ for Zr, and $2s^2 2p^4$ for O. The energy cutoff for the plane-wave basis set was set at 500 eV. Supercells consisting of 360 atoms were used for structural relaxation and energy calculations for $Ba_{1-x}Sr_xZrO_3$. Structural relaxation was conducted using Monkhorst–Pack *k*-point sets of $2 \times 2 \times 2$ until the total energy difference converged to less than 0.001 eV, which resulted in residual forces below 0.02 eV $Å^{-1}$. The total energies of the system were finally obtained using Monkhorst–Pack *k*-point sets of $5 \times 5 \times 5$, using a tetrahedron method with Blöchl corrections to obtain accurate total energies after structural relaxation.

2.4.2 Model structures of $Ba_{1-x}Sr_xZrO_3$. Supercells containing 360 atoms were prepared for x = 0, 0.25, 0.50, 0.75, 0.875, and 1. For the x = 0.25, 0.50, 0.75, and 0.875 models, Ba and Sr were set randomly at A-sites, to avoid segregation of $BaZrO_3$ and $SrZrO_3$ in the cell. The effects of the A-site configuration patterns were checked at x = 0.875 using a Ba distributed cell (Model 1), and a Ba clustering cell (Model 2). In Model 1, all of the A-sites nearest to Ba were occupied by Sr. In contrast, in Model 2, half of the nearest A-sites of Ba were occupied by Sr, and the other half were occupied by Ba. Full relaxation, including cell size and shape, was conducted for the supercell with x = 0, 0.25, 0.50, 0.75, 0.875, and 1.

3. Results and discussion

3.1 Composition analysis

The composition of the solid phase was obtained by measuring the concentration of ions in the filtrates using ICP-AES, and subtracting the amounts of ions in the filtrates from that in the starting solutions. Fig. 2 shows the relationship between the x values of the products and the feed solutions (x of $Ba_{1-x}Sr_xZrO_3$). It was confirmed that molar ratio in the products corresponded to that in the feed solution; the relationship was not perfectly linear, but was slightly nonlinear and curved.

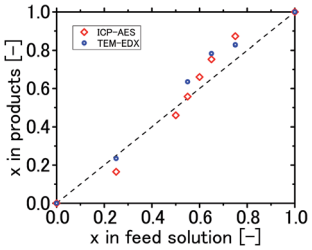

Fig. 2 Relationship between the x value of products and the feed solutions (x in $Ba_{1-x}Sr_xZrO_3$), measured using ICP-AES for filtrates (rhombuses), and TEM-EDX for each single nanoparticle (circles).

Composition analysis was also performed for every single nanoparticle using TEM-EDX, using a nano-size electron beam. From the single-particle composition analysis, it was confirmed that both Ba and Sr were included in every nanoparticle, except for $x = 0$ and $x = 1$. The relationship between x for the feed solution and x for the products was obtained using TEM-EDX, and the results are shown in Fig. 2. As shown in Fig. 2, the tendency of the x value determined using TEM-EDX analysis was very similar to the tendency determined using ICP-AES analysis. This showed that the results of the nano-scale TEM-EDX analysis were consistent with those obtained using the bulk ICP-AES analysis.

Fig. 3 shows the molar ratio of A-site ions per B-site ion, obtained using TEM-EDX. Plots show the averaged value of 20 measurements, and error bars show standard deviation of the measured values which were approximately 10–25% of (Ba + Sr)/Zr ratio. The existence of more A-site vacancies in $BaZrO_3$ ($x = 0$) was suggested, and fewer A-site vacancies were expected when the amount of Sr at the A-sites was increased. Basically, Sr is easier to incorporate into the structure as shown in Fig. 3 due to a smaller ionic radius of Sr than that of Ba. However, Fig. 2 shows that Ba is more incorporated specifically at $x = 0.25$, and we think that structure difference affected the incorporation (*i.e.* Ba is more incorporated into cubic perovskite, and Sr is more incorporated into orthorombic perovskite). This tendency was confirmed using ICP-AES for the filtrates and XPS for the nanoparticles, as shown in Fig. 4. It should be noted that the values obtained using XPS were always smaller than the values obtained using TEM-EDX; this outcome suggested the existence of a Zr-rich phase (*i.e.*, an A-site-defective phase), in the surface of the nanoparticles.

3.2 Crystal structure

XRD measurements and Rietveld refinements were conducted for the synthesized $Ba_{1-x}Sr_xZrO_3$. XRD data in the wide-angle region for each x value, and enlarged patterns for selected angles are shown in the ESI section.† Structural changes from $Pm\bar{3}m$ (cubic) to $I4/mcm$ (tetragonal) between $x = 0.25$ and $x = 0.50$, and from $I4/mcm$ (tetragonal) to $Pnma$ (orthorhombic) between $x = 0.55$ and $x = 0.60$, were observed. Fig. 5A–D show the Rietveld fitting results for the sample around the phase transition regions of $x = 0.25$ ($Pm\bar{3}m$), 0.50 ($I4/mcm$), 0.55 ($I4/mcm$), and 0.60 ($Pnma$); the results were refined with a high level of accuracy ($x = 0.25$: $S = 1.1260$, $R_F = 2.651$; $x = 0.50$: $S = 1.2709$, $R_F = 2.722$; $x = 0.55$: $S = 1.8267$, $R_F = 1.288$; $x = 0.60$: $S = 1.2994$, $R_F = 2.271$). Kennedy *et al.* investigated the structure of $Ba_{1-x}Sr_xZrO_3$ using synchrotron high-resolution XRD, and a phase diagram of $Ba_{1-x}Sr_xZrO_3$ was proposed after high-temperature powder diffraction studies.[31] The results of the Kennedy *et al.* study[31] showed that phase changes occurred in $Ba_{1-x}Sr_xZrO_3$ at 400 °C, at the following x values: $Pm\bar{3}m$ to $I4/mcm$ at $x = 0.4$, $I4/mcm$ to $Imma$ at $x = 0.6$, and $Imma$ to $Pnma$ at $x = 0.7$. The phase-change region in the composition investigated here was consistent with their measurements performed at 400 °C, indicating that no structural transformation occurred during cooling—and after recovery—in our experiments; the diffraction data measured at room temperature after recovery of the particles showed different behavior, compared with the phase diagram determined at room temperature ($Pm\bar{3}m$ to $I4/mcm$ at $x = 0.2$, $I4/mcm$ to $Imma$ at $x = 0.4$, $Imma$ to $Pnma$ at $x = 0.5$).

Fig. 6 illustrates the dependence of the lattice volume on the A-site composition; the lattice volume decreased with increases in x. The ionic radius of Ba^{2+} (142 pm) is larger than that of Sr^{2+} (126 pm), and the changes in the lattice parameter could be explained by the differences in the ionic radii. Fig. 6 also shows the lattice volume obtained *via* first-principles calculation. A decrease in lattice volume with increases in Sr was observed in both the experimental and the computational data, suggesting that both Ba and Sr were located at the A-sites of the perovskite, and that the presence of A-site ions significantly affected the

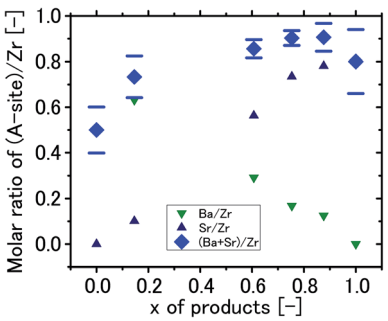

Fig. 3 Molar ratio of A-site ions (Ba + Sr) per B-site ion (Zr), obtained using TEM-EDX (rhombuses: (Ba + Sr)/Zr, up-triangles: Sr/Zr, down-triangles: Ba/Zr).

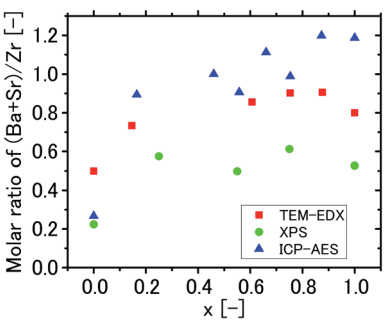

Fig. 4 Molar ratio of A-site ions (Ba + Sr) per B-site ion (Zr), obtained using ICP (triangles), XPS (circles), and TEM-EDX (squares).

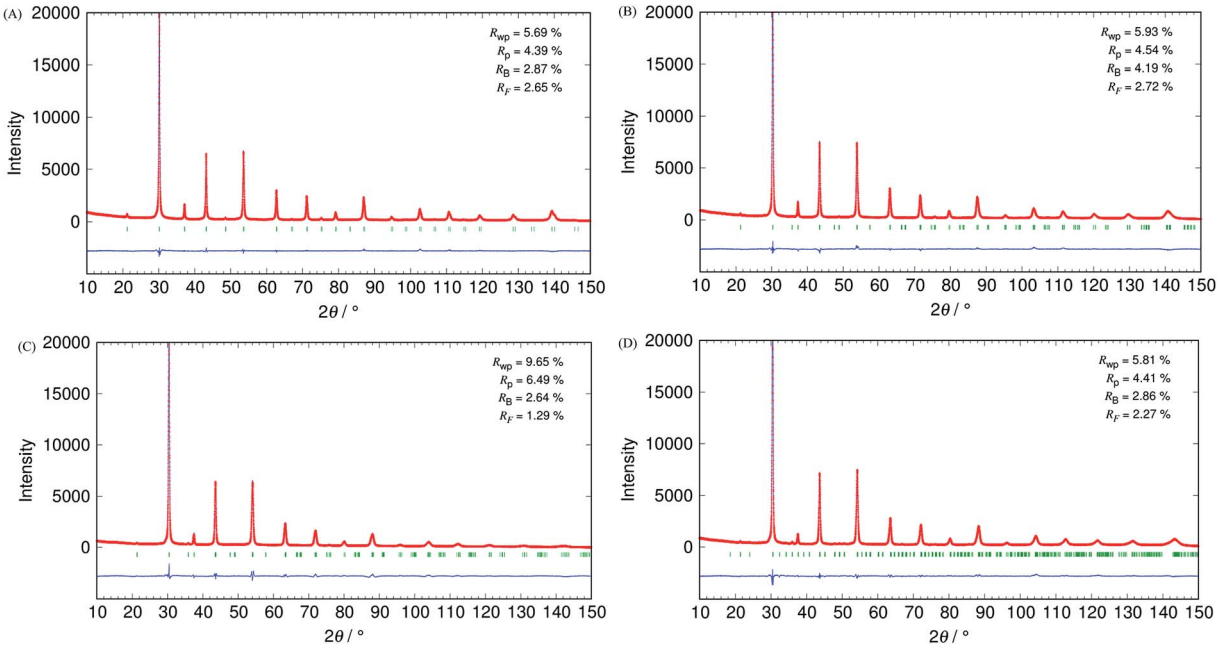

Fig. 5 Rietveld fitting results around the structural phase transition regions: (A) $x = 0.25$ ($Pm\bar{3}m$), (B) $x = 0.50$ ($I4/mcm$), (C) $x = 0.55$ ($I4/mcm$), (D) $x = 0.60$ ($Pnma$).

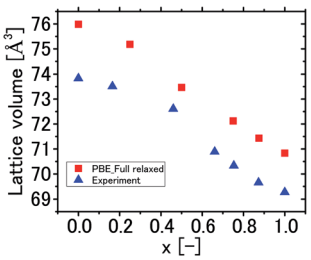

Fig. 6 Lattice volume for each x value, compared with values obtained using the DFT-PBE calculations, (squares) and values refined by Rietveld analysis (triangles).

lattice volume. A slight divergence from Vegard's law was observed in the experimental results, while the computational results with full relaxation clearly obeyed Vegard's law. The variance in lattice volume could have been caused by the difference in particle size; this is discussed in Section 3.4.

3.3 Local structure

In the previous section, it was shown that the presence of elements at the A-site had a significant effect on the crystal structure of $Ba_{1-x}Sr_xZrO_3$. The existence of many A-site vacancies was suggested by the compositional analysis, and it was important to analyze the defective local structure of the particles. EXAFS analysis was conducted to elucidate the local structure of the $Ba_{1-x}Sr_xZrO_3$, which had a defective structure. Fig. 7A shows the $k^3\chi(k)$ spectrum obtained from Zr K edge spectra. From the results, the spline range was set at 0–16 Å^{-1} in the wave number k. Fig. 7B shows the radial structure function obtained *via* a Fourier transform of the $k^3\chi(k)$ spectrum in the range of 3–14 Å^{-1} in k. The fitting range was set at 1.2–3.3 Å, to cover the first and second coordination in the radial structure function. The coordination number and coordination distance were obtained from this fitting. Structural information obtained using XRD was used as an initial model structure for the fitting. It was found that the number of oxygen atoms coordinated to zirconium did not vary when the composition ratio x was changed. In contrast, as shown in Fig. 8, the number of Ba atoms coordinated to Zr (second coordination) was significantly smaller than the number in a perfect crystal. In addition, the Ba-to-Zr coordination number increased with increases in x in $Ba_{1-x}Sr_xZrO_3$. The results confirmed the existence of many vacant A-sites in $Ba_{1-x}Sr_xZrO_3$, and a decrease in the number of vacancies with increases in Sr (*i.e.*, increases in x). This local structure analysis performed using EXAFS supported the results of the single-particle composition analysis performed using TEM-EDX. Many vacancies existed in the A-sites, whereas the coordination number of O-to-Zr, and the cation valence, did not change. These EXAFS results suggested that charge neutralization for the A-site deficiencies was compensated for by proton occlusion during the crystallization. Diffusion of Ba and Sr in the solid state was a possible cause for the differences in the concentration of vacancies with different x. Sr diffuses more easily than Ba, because of the difference in the ionic radii; the higher diffusibility of Sr could have resulted in a smaller number of vacancies in the case of larger x values.

3.4 Particle size

Fig. 9A shows the crystallite size at each x value, obtained using the Williamson–Hall equation:[32]

$$\beta^2(\cos\theta)^2 = X^2 + Y^2(\sin\theta)^2$$

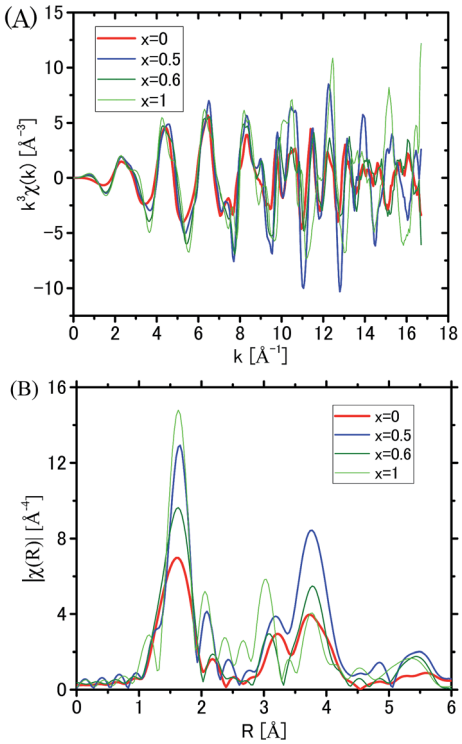

Fig. 7 (A) $k^3\chi(k)$ spectrum obtained from Zr K edge absorption spectrum; (B) radial structure function obtained *via* a Fourier transform of the $k^3\chi(k)$ spectrum.

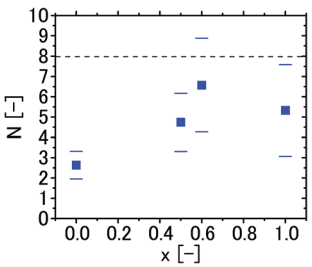

Fig. 8 Coordination numbers of Ba that second coordinated to Zr, obtained from the fitting for the radial structure function.

here, β and θ are the peak width and the angle of the diffraction peaks, Y represents peak broadening due to strain, and X is a factor representing peak broadening due to crystallite size. The peak became broader at larger detection angles, suggesting the effects of strain. We discriminated between the effects of strain and that of the size on peak broadening using the Williamson–Hall equation. Fig. 9A shows that the crystallite size of the $Ba_{1-x}Sr_xZrO_3$ increased with increases in x, and a significant difference in the size of $BaZrO_3$ (approximately 20 nm) and $SrZrO_3$ (approximately 60 nm) was observed. The particle size measured using TEM (as shown in Fig. 9B) was consistent with the XRD results, and it was confirmed that each particle grew larger with increases in x. Representative TEM images for x = 0 and 1 are shown in Fig. 10A. At the nanoscale, smaller particles have a larger lattice, and the difference in particle size might have caused the lattice variation shown in Fig. 6.

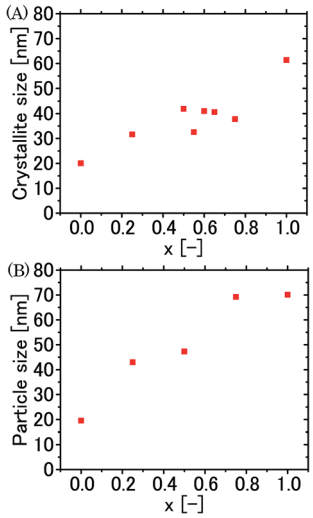

Fig. 9 (A) Crystallite size at each x value of $Ba_{1-x}Sr_xZrO_3$, obtained using the Williamson–Hall method. (B) Particle size of $Ba_{1-x}Sr_xZrO_3$ observed using TEM.

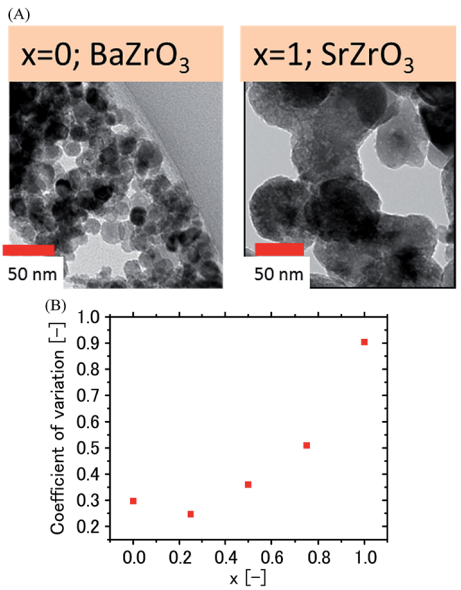

Fig. 10 (A) TEM images for x = 0 and x = 1; (B) coefficient of variation of particle size observed by TEM.

The composition of the A-sites influenced the particle size, although the B-site Zr has a dominant role at nucleation stage (*i.e.*, Zr precipitated faster than the A-site ions, because of the much lower solubility of the Zr, and A-site ions were taken up into the particles after the Zr nucleation). It was therefore suggested that the particle size was determined not only by the nucleation of Zr, but also by the subsequent stage involving the formation of the composite oxide phase.

It should be noted that, here, "subsequent stage" does not refer to Ostwald ripening. When a particle grows *via* Ostwald ripening, the particle size distribution tends to become narrower with increases in particle size; however, such a tendency

was not observed in our TEM observations, as demonstrated by the x-dependence of the coefficient of variation for the particle size in Fig. 10B. Considering that each particle was a monocrystal, it was suggested that the growth could have been related to the coalescence of nuclei, which occurs only at the early stage of crystallization, when each particle has enough deformable structure to grow as a result of collisions with other particles.

3.5 Surface state

Elucidating the factors determining the particle size are important for understanding the mechanism of formation of nanoparticles, and to find a way to control the size of nanoparticles. We examined the surface state of the synthesized $Ba_{1-x}Sr_xZrO_3$, where the surface state could be related to the particle size.

Philippot *et al.* synthesized $Ba_{1-x}Sr_xTiO_3$ in supercritical water, and suggested that the surface state, particularly the hydroxyl groups (–OH) on the particle surface, had some influence on the increase in particle size. They concluded that the concentration of surface-OH can be regarded as an index for ripening.[33] Here, XPS analysis was conducted to investigate whether the difference in particle size could be attributed to the surface density of –OH in this case. First, the peak positions in the O 1s spectra were calculated, and peak-fitting analysis was then conducted to elucidate the differences in surface state.

First-principles calculations were conducted to confirm the relationship between crystal structure and the shift in binding energy for each sample. The core level shift of O 1s was obtained using an initial state approximation implemented in VASP.[34] The Kohn–Sham energy of the core states was obtained, and the core level shift was calculated referring to the Fermi level, as shown in the following equation:

$$\begin{aligned}\Delta E(\text{core level shift}) = &(\varepsilon_{O1s}(x = 0.25, 0.50, 0.75, 0.875, \text{and } 1) \\ &- \varepsilon_F(x = 0.25, 0.50, 0.75, 0.875, \text{and } 1)) \\ &- (\varepsilon_{O1s}(x = 0) - \varepsilon_F(x = 0)) \quad (1)\end{aligned}$$

where ε_{O1s} and ε_F are the energy eigenvalues of the oxygen 1s state and the Fermi level, respectively, in each compound. We used the averaged values of the O 1s core state energy level because not all of the oxygen sites were equivalent in $Ba_{1-x}Sr_xZrO_3$. The screening and relaxation of valence electrons for the core hole was neglected here, and a qualitative interpretation was conducted.

Fig. 11 shows the experimental binding energy difference and simulated core level shift in O 1s for each x in $Ba_{1-x}Sr_xZrO_3$. From the results, it was confirmed that structural differences resulting from changes in x caused the shifts in the binding energy. The abrupt drop in the core level shift around $x = 0.75$ observed in the experimental results might have originated from the local atomic displacement. Fig. 11 also shows computational results achieved using atomic positions determined using diffraction data (denoted as unrelaxed structure in the following); a similar inverse shift was observed at $x = 0.75$. To analyze this phenomenon, the distortion index proposed by Baur[35] for the ZrO_6 polyhedron was estimated for the full

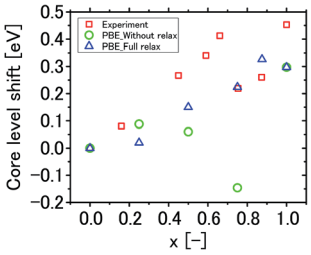

Fig. 11 Core level shift of O 1s for each x for $Ba_{1-x}Sr_xZrO_3$ obtained by XPS (squares), DFT-PBE without relaxation (circles), and DFT-PBE with full relaxation (triangles).

relaxed structure, 0.0047, and for the unrelaxed structure, 0.0366, at $x = 0.75$. The distortion index represented the variance of the bond length, and the larger the index, the more distortion remained in the structure, indicating that the unrelaxed structure held a larger amount of distortion. Because the abrupt drop in the core level shift at $x = 0.75$ was observed in the computational results with unrelaxed structure, and in the experimental results, we conclude that the products at $x = 0.75$ were subject to larger distortion in the crystal, and that the local distortion led to the irregular shift in binding energy. In addition, it was confirmed that the effects of the A-site configuration on the core level shift were negligible, from the comparison of the results given by two different configuration models (Model 1 and Model 2). These simulations provided a validation for the shift in peak positions in our peak separation fitting for the surface-OH and structural-O.

Fig. 12 shows the O 1s peaks of the XPS spectra for each x, after subtraction of the background, with three fitting curves for bulk-O (528.5–529.2 eV), surface-OH (530.3–531.1 eV), and absorbed water (531.6–533.0 eV). Multi-peak fitting was conducted, to divide peaks into the three components using the Voigt function.

Fig. 13 shows the peak area ratio of surface-OH to structural-O at each x value, obtained *via* the fitting. In contrast with the previous study by Philippot *et al.*,[33] the density of surface-OH decreased with increases in the molar ratio of Sr, *i.e.*, the increase in particle size. In this case, the difference in particle size could not be explained by the higher density of surface-OH; rather, it is likely that collision growth was prevented by the larger repulsive forces resulting from the high density of

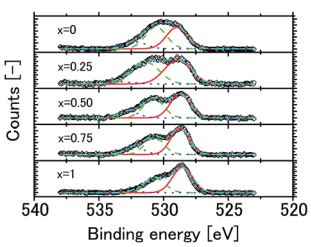

Fig. 12 O 1s peaks of XPS spectra after subtracting background, for each x ($x = 0$, $x = 0.25$, $x = 0.50$, $x = 0.75$, and $x = 1$ from top to bottom), with fitting curves (solid line: structural-O, dashed line: surface-OH, and dotted line: absorbed water).

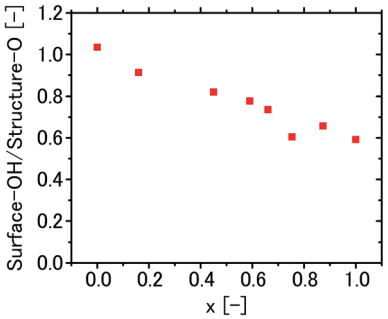

Fig. 13 Intensity ratio of surface-OH per structural-O, obtained using the fitting results at each x value.

surface-OH. A higher concentration of A-site deficiencies and a higher density of surface-OH was observed under Ba-rich conditions; it is believed that the charge neutrality for the A-site deficiencies was compensated for by the inclusion of protons in the crystal, as mentioned in Section 3.3. Further study of the structural formation, considering in particular the surface structure of the nanoparticles, is required to elucidate the growth mechanism and utilize these nanoparticles as new materials.

4. Conclusions

In this study, nanoparticle formation under highly supersaturated conditions that accelerated nucleation was studied using supercritical water.

The formation of nanoparticles of $Ba_{1-x}Sr_xZrO_3$ $(0 \leq x \leq 1)$ during supercritical hydrothermal synthesis was investigated for the first time. Composite oxides including both Ba and Sr at the A-sites were obtained, and it was found that the A-site composition greatly affected the crystal structure, particle size, vacancy concentration, and surface state. A-site ions played a particularly important role in determining the particle size. High concentrations of A-site deficiencies and a corresponding increase in surface-OH in Ba-rich products were related to the prevention of particle growth. In addition, it is plausible that the diffusibility of A-site ions in the solid determined the concentration of A-site vacancies, and that protons compensated for the charge of the A-site deficiencies, resulting in increases in the concentration of surface-OH with the increases in the number of A-site deficiencies.

Regarding the supercritical hydrothermal synthesis of zirconate, zirconium precipitation is so rapid that all zirconium ions turn into a solid phase at an early stage of crystallization, due to the extremely low solubility of zirconium in supercritical water. Following the Zr nucleation, the crystallization in the particles proceeds, and a composite oxide phase is formed *via* the uptake of Ba and Sr. In this model, Zr, which has a lower solubility, takes a leading role in the nucleation and growth. However, in this study it was found that the zirconate particle size differed depending on the A-site composition. The difference in the particle size could not be explained sufficiently by considering only Zr nucleation and A-site ion (Ba, Sr) uptake. This indicated that a subsequent process of particle growth following the nucleation process, such as ripening or coalescence, was a key phenomenon in controlling the particle size. The investigation of the particle size variance indicated that a coalescence mechanism occurring only at the early stages of crystallization was plausible. Abundant A-site deficiencies and surface-OH could have prevented collision particle growth. It was concluded that the coalescence mode in the early stages of crystallization affected the products, even under highly supersaturated conditions in supercritical water, which accelerated nucleation and inhibited growth.

Acknowledgements

This work was performed using the facilities of the Institute for Solid State Physics, The University of Tokyo (XRD, TEM, ICP), and the Institute of Engineering Innovation, The University of Tokyo (XPS). The XAFS experiments were performed at the BL9C, PF, with the approval of the KEK (Proposal No. 2013G555). First-principles calculations were conducted using the super-computing system of the National Institute for Materials Science (NIMS). Our discussions with Professors T. Adschiri, E. Lester, and C. Aymonier who have done pioneering work in supercritical hydrothermal synthesis are greatly appreciated.

References

1 S. H. Lee, J. I. Choi, Y. J. Kim, J. K. Han, J. Ha, E. Novitskaya, J. B. Talbot and J. McKittrick, *Mater. Charact.*, 2015, **103**, 162–169.
2 C. C. Yang, Y. C. Chen and Y. C. Liao, *Mater. Res. Bull.*, 2012, **47**, 2616–2622.
3 A. Abdullah, A. S. Saleemi and M. Anis-ur-Rehman, *J. Supercond. Novel Magn.*, 2013, **27**, 273–276.
4 Y. L. Cui, W. J. Bao, Z. Yuan, Q. C. Zhuang and Z. Sun, *J. Solid State Electrochem.*, 2012, **16**, 1551–1559.
5 H. Y. He, *J. Mater. Sci.: Mater. Electron.*, 2012, **23**, 995–1000.
6 H. B. Zhao, D. F. Mei, J. C. Ma and C. G. Zheng, *Asia-Pac. J. Chem. Eng.*, 2014, **9**, 610–622.
7 T. Adschiri, Y. Hakuta, K. Sue and K. Arai, *J. Nanopart. Res.*, 2001, **3**, 227–235.
8 H. Hayashi and Y. Hakuta, *Materials*, 2010, **3**, 3794–3817.
9 A. Yoko, M. Akizuki and Y. Oshima, *J. Nanopart. Res.*, 2014, **16**, 2330.
10 A. Yoko, M. Akizuki, N. Hirao, S. Kohara, M. Kumar, N. Umezawa, T. Ohno and Y. Oshima, *J. Supercrit. Fluids*, 2016, **107**, 746–752.
11 K. Sue, M. Aoki, T. Sato, D. Nishio-Hamane, S. Kawasaki, Y. Hakuta, Y. Takebayashi, S. Yoda, T. Furuya, T. Sato and T. Hiaki, *Ind. Eng. Chem. Res.*, 2011, **50**, 9625–9631.
12 H. Iwahara, T. Yajima, T. Hibino, K. Ozaki and H. Suzuki, *Solid State Ionics*, 1993, **61**, 65–69.
13 T. Sugimoto, S. Hasegawa and T. Hashimoto, *Thermochim. Acta*, 2012, **530**, 58–63.
14 T. Sugimoto and T. Hashimoto, *Electrochemistry*, 2014, **82**, 833–838.

15 W. F. F. W. Ali, N. A. Rejab, M. Othman, M. F. Ain and Z. A. Ahmad, *J. Sol–Gel Sci. Technol.*, 2012, **61**, 411–420.
16 L. B. Kong, S. Li, T. S. Zhang, J. W. Zhai, F. Y. C. Boey and J. Ma, *Prog. Mater. Sci.*, 2010, **55**, 840–893.
17 A. Dixit, D. C. Agrawal, Y. N. Mohapatra, S. B. Majumder and R. S. Katiyar, *Mater. Lett.*, 2007, **61**, 3685–3688.
18 C. J. Howard, K. S. Knight, B. J. Kennedy and E. H. Kisi, *J. Phys.: Condens. Matter*, 2000, **12**, L677–L683.
19 T. Sugimoto and T. Hashimoto, *IOP Conf. Ser.: Mater. Sci. Eng.*, 2011, **2**, 022007.
20 R. Terki, G. Bertrand, H. Aourag and C. Coddet, *J. Alloys Compd.*, 2008, **456**, 508–513.
21 Y. Zhu, Z. G. Chen, W. Zhou, S. Jiang, J. Zou and Z. Shao, *ChemSusChem*, 2013, **6**, 2249–2254.
22 C. Zhang and H. Zhao, *Mater. Res. Bull.*, 2010, **45**, 1659–1663.
23 K. Imaki, M. Nakayama, Y. Uchimoto and M. Wakihara, *Solid State Ionics*, 2004, **172**, 73–76.
24 M. Nakayama, K. Imaki, Y. Uchimoto and M. Wakihara, *Solid State Ionics*, 2004, **172**, 77–80.
25 D. Wang, R. Yu, S. Feng, W. Zheng, R. Xu, N. Kumada and N. Kinomura, *Mater. Res. Bull.*, 2001, **36**, 239–244.
26 S. I. Kawasaki, K. Sue, R. Ookawara, Y. Wakashima, A. Suzuki, Y. Hakuta and K. Arai, *J. Supercrit. Fluids*, 2010, **54**, 96–102.
27 F. Izumi and K. Momma, *Solid State Phenom.*, 2007, **130**, 15–20.
28 B. Ravel and M. Newville, *J. Synchrotron Radiat.*, 2005, **12**, 537–541.
29 G. Kresse and J. Furthmüller, *Phys. Rev. B: Condens. Matter Mater. Phys.*, 1996, **54**, 11169–11186.
30 J. P. Perdew, K. Burke and M. Ernzerhof, *Phys. Rev. Lett.*, 1996, **77**, 3865–3868.
31 B. J. Kennedy, C. J. Howard, G. J. Thorogood and J. R. Hester, *J. Solid State Chem.*, 2001, **161**, 106–112.
32 G. K. Williamson and W. H. Hall, *Acta Metall. Mater.*, 1953, **1**, 22–31.
33 G. Philippot, K. M. Ø. Jensen, M. Christensen, C. Elissalde, M. Maglione, B. B. Iversen and C. Aymonier, *J. Supercrit. Fluids*, 2014, **87**, 111–117.
34 L. Köhler and G. Kresse, *Phys. Rev. B: Condens. Matter Mater. Phys.*, 2004, **70**, 165405.
35 W. H. Baur, *Acta Crystallogr., Sect. B: Struct. Crystallogr. Cryst. Chem.*, 1974, **30**, 1195–1215.